Kemal Aziz

$E = mc^2$ High School Journal Submission

Our ancestors lived out life like ants on an anthill—unable to sense their presence in an ecosystem greater than themselves. While Earth is still our anthill, a tiny speck of dust practically indistinguishable from infinitely many others, reading Brian Greene's "The Elegant Universe" at age nine taught me that we can escape the ignorance of ants. Here, I realized that "superstring theory"—describing all matter as vibrations of tiny superstrings—required the existence of seven extra spatial dimensions physically impossible for us to perceive.

In my elementary school yearbook, next to my name, is "When I grow up, I would like to be: A Physicist". Physics is not the sole realm of mathematical geniuses, but those who seek to experience worlds, physical realities so foreign yet so real. Previously, underlying philosophical questions—What is our fate? —were relegated to individuals like Socrates. Studying the farthest of superclusters, the tiniest of superstrings, and everything in-between, enables us to discover our place in the cosmos.

Quantum Field Theory—describing coupled systems as objects of an underlying field—is the most universal physical theory ever constructed which possesses stringent experimental verification. As both a high school sophomore and aspiring theorist, I was amazed that a mathematical framework could accurately predict the magnetic moment of an electron to eleven decimal places. As such, I contacted and immediately began collaboration with Brooklyn College's condensed matter group under the advisement of Dr. Karl Sandeman. The topic of my work was modelling the crystal structure of magnetic alloys (e.g., CoMnSi and GdCo) on an atomic scale using the MATLAB library SpinW, generating simulated magnetic flux data using the C++ library VAMPIRE, and automating Python-based comparison of thermodynamic outputs (e.g., entropy and temperature changes) with experimental data.

A theme prevalent throughout condensed matter physics is that microscopic fluctuations manifest as macroscopic behaviors. GdCo, for instance, exhibits the "magnetocaloric effect", whereby the application of a magnetic field induces temperature changes in certain alloys, currently subject to ongoing research by General Electric. The Heisenberg Spin Hamiltonian is an operator used to calculate the total energy of a magnetic system, given matrices which represent "spin" magnetic moments of constituent, interacting atoms within a lattice. Geometric structures called space groups yield the periodic configuration of such a lattice in space, dependent on the material modelled. In SpinW, I used existing space group parameters to understand how these temperature changes emerged from atomic-scale interactions. The tensor transformation law is a property specifying how many-component objects (e.g., vectors) evolve under rotations. Using VAMPIRE algorithms, we modelled the switching, or "phase transition", of magnetic states by mapping a temperature evolution of spins whose matrix elements may also be treated as vector components.

Performing this work, realized that the human mind cannot physically visualize the motion of magnetic interactions as it perceives leaves falling off a tree, for example. To compensate, I learned about the interface between perceptive observables (e.g., magnetically-induced temperature changes in materials) and the unobservable (e.g., subatomic magnetic interactions), employing mathematical relations in transforming experimental data into a better understanding of these two scales. Integrating multiple laws to describe a single magnetic system sparked my fascination on the interplay between mathematics and physical reality.

This fascination led me to study the Maxwell Relations, which mathematically relate different thermodynamic potentials like pressure and temperature. Here, I interpreted the symmetry of second derivatives as one essential to quantify observable changes in magnetic entropy. Akin to the distributive property of addition, there exist cyclic relationships among differentiating the same functions in different orders which obey the "Schwarz Theorem". Given that we know how the temperature of an object varies with respect to entropy while volume is held constant, for instance, we can also quantify entropy as a function of volume. This work "brings to life" the textbook-based Maxwell Relation and Heisenberg Spin Hamiltonian, which describe

incremental changes of magnetic behavior on large and small scales, respectively, by quantifying real-world systems.

Unfortunately, only rarely do theorists make breakthroughs, and the most successful sustain a level of grit which is superhuman. Before trying to replicate Einstein's Annus Mirabilus, I recommend using Gerald Hooft's online "How to be a Good Theoretical Physicist" as a course outline, or the book "Quantum Field Theory for the Gifted Amateur" to gain an extremely solid knowledge base. You should not only learn what you cannot in class, but also understand the limits of your own mind. I recall a time on an AP Physics test where I scored a 2/15 on a free response question concerning circuits. Likewise, by self-confession, Einstein was only a mediocre mathematician, but read Immanuel Kant's "Critique of Pure Reason" to study how humans reasoned. In satiating your mind to its full capacity, you will discover what no one else can.

In pursuing an underlying structure driving the universe, one discovers elegance by contextualizing the human experience against the forces which master our destiny.

Research Abstract

The magnetocaloric effect (MCE) is the temperature change of a magnetic material induced by exposing the material to a varying external magnetic field. The primary industrial application of the MCE is magnetic refrigeration, which is already used to achieve very low temperatures (below 4 degrees Kelvin) and has the potential to replace conventional refrigerators for domestic use. For high cooling device efficiency, a substantial change of magnetic entropy (ΔS) coupled with a high refrigerant capacity (RC) is desirable. The objective of this project is to compare a conventional magnetocaloric alloy (La-Fe-Si) and an inverse magnetocaloric alloy (CoMnSi) in terms of cooling efficiency. Both datasets were generated by using a Vibrating Sample Magnetometer (VSM) to obtain magnetization as a function of temperature and applied magnetic field. Entropy change (ΔS), RC as a function of applied field, hysteresis curves, gradient plots and 3D visualization plots are incorporated to carry out a novel comparison of material behavior, based on literature data consisting of measurements of the materials' magnetization at different temperatures given a varying magnetic field. La-Fe-Si loses magnetic entropy upon the application of a magnetic field while CoMnSi gains magnetic entropy upon the application of a magnetic field. As expected, La-Fe-Si has a much larger refrigerant capacity and entropy change than CoMnSi at similar applied magnetic fields. This analysis culminates in a set of software tools built at an interface between MATLAB, C++, and Python to both classify emergent magnetization as a function of spin fluctuations described by the Heisenberg Spin Hamiltonian and yield a set of mathematical tools to aid in the analysis of experimental magnetization data from other materials in the future.

Kemal Aziz

Introduction

The conventional magnetocaloric effect (MCE) occurs when the temperature of a magnetocaloric material (MCM) increases when it is exposed to a magnetic field and decreases when it is removed from it. This is also known as cooling by adiabatic demagnetization (Smith, 2013). When observed in large magnitudes, this is also known as the Giant Magnetocaloric Effect (G-MCE) (Krenke et al., 2005). The primary MCMs include rare-earth ferromagnets such as Gadolinium (Gd) and Heusler ferromagnetic alloys containing transition metals such as Iron (Fe), Cobalt (Co) and Manganese (Mn) (Guillou, Porcari, Yibole, Dijk, & Brück, 2014). The MCE is intrinsic to all magnetic materials but the magnitude of the effect and the Curie temperature (TC) varies widely between different magnetic materials. The Curie temperature is defined as the point where a ferromagnetic material becomes paramagnetic due to increasing thermal fluctuations (Pecharsky & Gschneidner, 1999). While a ferromagnetic substance has the magnetic moments of its atoms aligned, a paramagnetic substance has its magnetic moments in random directions (Kochmański, Paszkiewicz, & Wolski, 2013). The largest MCE occurs in materials that have a sharp change of lattice parameters and structure type at magnetic phase transition points, such as at the TC (Kochmański et al., 2013).

The inverse MCE occurs when a magnetic material cools down under an applied magnetic field in an adiabatic process. As opposed to the conventional MCE, the inverse MCE occurs when a magnetic field is applied adiabatically, rather than removed, and the sample cools (Krenke et al., 2005). Hence, this is also known as cooling by adiabatic magnetization. Adiabatic demagnetization is the process by which the removal of a magnetic field from magnetic materials lowers their temperature (Khan, Ali, & Stadler, 2007). The inverse MCE is very rare in all materials; however, it is known that transition metals such as silicon (Si) can be used to tune alloys to induce the inverse MCE (Krenke et al., 2005). The inverse MCE can be observed in materials where first order magnetic transitions from antiferromagnetic to ferromagnetic (AF/FM) or from antiferromagnetic to ferrimagnetic states (AF/FI) take place (Khan et al., 2007). First order transitions are characterized by a discontinuous change in entropy at a fixed temperature, such as most solid–liquid and liquid–gas transitions. On the other hand, second order transitions occur when there is a continuous change in entropy, such as metal-superconductor transitions (Schekochihin, n.d.).

There are several different quantities for evaluating the performance of an MCM which can be derived from magnetization measurements. Two key quantities are magnetic entropy change and refrigerant capacity (RC) (Guillou et al., 2014). Magnetic entropy change can be determined by first finding the rate of change in magnetization (derivative of magnetization) with respect to temperature while the applied field is held constant. Then ΔSM is found by calculating the area under curve, or definite integral, of this derivative at different temperatures given a constant starting temperature (Franco, n.d.). RC is defined as the amount of heat transferred between cold and hot reservoirs. RC can be calculated as the temperature integral of magnetic entropy change. The cold and hot reservoirs are temperatures corresponding to the full width at

half maximum (FWHM) of the peak entropy change (Franco, n.d.). Lastly, magnetic hysteresis losses occur when magnetic induction lags the magnetizing force. First-order magnetic materials display elevated levels of hysteresis losses (Franco, V., Blázquez, J. S., Ingale, B., & Conde, A., 2014).

The excitations of coupled spin systems form the basis of magnetism in condensed matter. The two primary interaction mechanisms for spins are magnetic dipole-dipole coupling and exchange interactions of quantum mechanical origin between localized electron magnetic moments (Cornell University, n.d.). Quantized spin waves, also known as magnons, are time-dependent phenomena based on the precession of these spin interactions through force carriers (Cornell Physics, n.d.). The Pauli Exclusion Principle, which states that two or more fermions cannot occupy the same state in a quantum system, is implemented to determine the spatial and spin coordinates of fermions, electrons in this case (Appelbaum, Huang, & Monsma, 2007). The wave function for the joint state of a magnetic interaction is a product of single electron states with respect to a symmetric or asymmetric magnetic interaction (Blundell, 2014). This change in electron states forms the basis of the Heisenberg Spin Hamiltonian, used in the determination of magnetic spin wave spectrums in many-body states, such as interactions between several intermittent electrons (Blundell, 2014).

The magnetically sensitive transistor may be developed because of research on the ability of electrons and other fermions to naturally possess one of two states of spin: spin up or spin down (Cheng, Daniels, Zhu, & Xiao, 2016). Unlike the common transistor, operating on an electric current, spin transistors operate on states of spin to store information in a binary manner (Sheremet, Kibis, Kavokin, & Shelykh, 2016). This ensures that spin states are detected and changed without requiring the constant application of an electric current (Appelbaum et al., 2007), enabling elimination of complex electronic components such as amplifiers.

Magnetic refrigeration is an alternative to conventional vapor compression/expansion systems, requiring a solid magnetocaloric material as the refrigerant (Du & Du, 2005). Today, there are an estimated 65 prototypes in existence, but the technology is not yet commercially available (Kitanovski, Plaznik, Tomc, & Poredoš, 2015). As opposed to vapor compression systems, magnetic refrigeration technology has no Ozone Depletion Potential (ODP) and little Global Warming Potential (GWP) as vapors are not used in the system. Energy demands for refrigeration and air conditioning account for approximately 20% of the world's energy consumption (Kitanovski et al., 2015).

Investigation of the Maxwell Definition for Entropy by Proof

The Maxwell integral for calculating entropy change, $\Delta S(T, \Delta H) = \int_0^{\Delta H} \left(\frac{\partial M}{\partial T}\right)_H dH$, is derived from the original Maxwell Relations, specifically the differential form of internal energy. The Maxwell Relations are a set of equations in thermodynamics which are derivable from the symmetry of second derivatives as well as from the definitions of thermodynamic potentials (Addison, n.d.). The Maxwell Relations express four basic thermodynamic quantities in terms of their natural variables, as shown in Eqs. (1.1-1.4) and Table 1.

The Maxwell Relations state:

$$+\left(\frac{\partial T}{\partial V}\right)_S = -\left(\frac{\partial P}{\partial S}\right)_V = \frac{\partial^2 U}{\partial S \partial V} \text{ (1.1)} + \left(\frac{\partial T}{\partial P}\right)_S = +\left(\frac{\partial V}{\partial S}\right)_P = \frac{\partial^2 H}{\partial S \partial P} \text{ (1.2)}$$

$$+\left(\frac{\partial S}{\partial V}\right)_T = +\left(\frac{\partial P}{\partial T}\right)_V = -\frac{\partial^2 F}{\partial T \partial V} \text{ (1.3)} - \left(\frac{\partial S}{\partial P}\right)_T = +\left(\frac{\partial V}{\partial T}\right)_P = \frac{\partial^2 G}{\partial T \partial P}. \text{(1.4)}$$

Thermodynamic Quantity	**Natural Variables**
U (internal energy)	S (entropy), V (volume)
H (enthalpy)	S (entropy), P (pressure)
G (Gibbs Energy)	T (temperature), P (pressure)
A (Helmholtz Energy)	T (temperature), V (volume)

Table 1. Nomenclature of thermodynamic quantities and their respective natural variables.

We start with a basic form of internal energy:

$$dU = TdS - pdv \text{ (2.1)}$$

$$T = \left(\frac{\partial V}{\partial S}\right)_V, -P = \left(\frac{\partial U}{\partial V}\right)_S \text{ (2.2)}$$

$$\frac{\partial}{\partial V}\left(\frac{\partial U}{\partial S}\right)_V = \frac{\partial}{\partial S}\left(\frac{\partial U}{\partial V}\right) \text{ (2.3)}$$

$$\left(\frac{\partial T}{\partial V}\right)_S = -\left(\frac{\partial P}{\partial S}\right)_V. \text{(2.4)}$$

This derivation applies to the other three basic thermodynamic relations as shown in Eqs. (2.2-2.4). Mathematically, any relation, thermodynamic or otherwise, in in the form of $dz = Mdx + Ndy$ may be simplified to $M = \left(\frac{\partial z}{\partial x}\right)_y, N = \left(\frac{\partial z}{\partial y}\right)_x$.

Now, we will introduce a new variable, M. In this case, internal energy (U) is not only a function of S and V but is also a function of magnetization, M (Maxwell Relation, 2013). This differential form of internal energy can now be written as:

$$dU = TdS - pdV + HdM. \text{(3.1)}$$

Applying this to Gibbs Free Energy results in:

$$G = U + pV - TS - MH. \text{(3.2)}$$

The differential form of Gibbs Free Energy becomes:

$$dG = dU + pdV + V\,dp - T\,dS - SdT - M\,dH - HdM. \text{(3.3)}$$

Substituting internal energy, we get:

$$dG = -SdT + Vdp - MdH. (4.1)$$

Eq. 4.1 expresses the total change of Gibbs free energy as a function of parameters *S*, *V,* and *M* and the differential changes in *T*, *p*, and *H* (Maxwell's Relations, n.d.). Meanwhile, the total differential forms of Gibbs Free Energy, G (*T, p, H*) and entropy, S (T, *p*, H) are:

$$dG = \left(\frac{\partial G}{\partial T}\right)_{p,H} dT + \left(\frac{\partial G}{\partial p}\right)_{T,H} dp + \left(\frac{\partial G}{\partial H}\right)_{p,T} dH \ (4.2)$$

$$dS = \left(\frac{\partial S}{\partial T}\right)_{p,H} dT + \left(\frac{\partial S}{\partial p}\right)_{T,H} dp + \left(\frac{\partial S}{\partial H}\right)_{p,T} dH. (4.3)$$

Since we assume that *dT=dP=0* in isothermal-isobaric (M.I.T., 2013) or closed systems, $\boldsymbol{dS} = \left(\frac{\boldsymbol{\partial S}}{\boldsymbol{\partial H}}\right)_{\boldsymbol{p,T}} \boldsymbol{dH.}$ (4.4)

Comparing coefficients in Eqs. (4.3) and (4.4) leads to the following expression for *S*, *M*, and *V:*

$$S(T,H,p) = -\left(\frac{\partial G}{\partial T}\right)_{p,H} (5.1)$$

$$M(T,H,p) = -\left(\frac{\partial G}{\partial T}\right)_{p,T} (5.2)$$

$$\mathrm{V\ (T,H,p)} = \left(\frac{\partial G}{\partial p}\right)_{T,H} (5.3)$$

Now, we can apply the Schwarz' Theorem of the symmetry of mixed partials in Eq. (1.1) to Eqs. (5.1-5.3). The Schwarz' Theorem states the following (Gutenberg, n.d):

$$\frac{\partial}{\partial y}\left(\frac{\partial f}{\partial x}\right) = \frac{\partial}{\partial x}\left(\frac{\partial f}{\partial y}\right) = \frac{\partial^2 f}{\partial x \partial y} = \frac{\partial^2 f}{\partial y x}$$

Substituting the thermodynamic potential *G* for *f* gives us

$\left(\frac{\partial}{\partial y}\left(\frac{\partial G}{\partial x}\right)\right)_{y,z} = \left(\frac{\partial}{\partial x}\left(\frac{\partial G}{\partial y}\right)\right)_{x,z}$ (Gutenberg, n.d). Based on the Schwarz' Theorem, the following symmetrical Maxwell Relations are formed in Eqs. (6.1-6.3):

$$\left(\frac{\partial S}{\partial p}\right)_{T,H} = -\left(\frac{\partial V}{\partial T}\right)_{p,H} (6.1)$$

$$\left(\frac{\boldsymbol{\partial S}}{\boldsymbol{\partial H}}\right)_{\boldsymbol{T,p}} = \left(\frac{\boldsymbol{\partial M}}{\boldsymbol{\partial T}}\right)_{\boldsymbol{p,H}} (6.2)$$

$$\left(\frac{\partial V}{\partial H}\right)_{T,p} = -\left(\frac{\partial M}{\partial p}\right)_{T,H} \quad (6.3)$$

We can substitute $(\frac{\partial M}{\partial T})_{p,H}$ for $(\frac{\partial S}{\partial H})$ in Eq. (4.4) to get $dS = (\frac{\partial M}{\partial T})_{p,H}\, dH$. Therefore, the Maxwell Relation for entropy change can now be written in its integral form:

$$\boxed{\Delta S_T = \int_{H_1}^{H_2} (\frac{\partial M}{\partial T})_{p,H}\ dH.} \quad (7.1)$$

Experimental Goals & Methods

Magnetization data is analyzed to compare the conventional MCE in $La(Fe,Si)_{13}H_\delta$, or La-Fe-Si, to the inverse MCE in CoMnSi. $La(Fe,Si)_{13}H_\delta$ notation is indicative of the 1:13 ratio in *La* to *Fe,Si* and relatively small concentrations of hydrogen: $\delta<2$ in H_δ. CoMnSi samples studied here were formed by comelting *Co (99.95%)*, Mn (*99.99%),* and *Si (99.9999%)* in equal ratio.

The expected outcome is that La-Fe-Si has a high potential for use in refrigeration applications while CoMnSi will demonstrate lesser potential for use in refrigerant applications. This is because conventional magnetocaloric alloys generally demonstrate a greater magnitude of the effect than less studied inverse alloys. However, an analysis of the inverse magnetocaloric behavior of CoMnSi will provide insight on ways to optimize inverse magnetocaloric materials for industrial applications. The primary goal is to understand how the magnetization behavior of CoMnSi varies from La-Fe-Si and how this difference translates to the suitability of industrial applications. To fulfill this goal, we transform magnetization data as a function of temperature and applied magnetic field into indicators of the MCE. Examples of these indicators are three-dimensional (3D) surface plots, hysteresis curves, refrigerant capacity (RC) plots, and magnetic entropy change curves. We apply the correlated relationship between material properties and refrigerator performance to provide insight on device operation. In refrigeration technologies, for instance, device operation is narrowly focused around the peak of the entropy curve.

Literature data were used as a part of this component of the study. The novel perspective of my research is comparing the conventional and inverse magnetocaloric effect, as these sets of data have not previously been used for this purpose. To enable me to analyze the conventional and inverse MCE, Dr. Karl Sandeman at Brooklyn College provided me with raw magnetization data from previous experiments. Data for La(Fe,Si)13H_δ were obtained from Vacuumschmelze GmbH & Co. KG (2015) while Dr. Sandeman's former Ph.D. student Alex Barcza measured data for CoMnSi (Barcza, et al., 2013). The mathematical analyses implemented with these data were primarily conducted in MATLAB and Python.

Both datasets were generated by using a Vibrating Sample Magnetometer (VSM) to obtain magnetization as a function of temperature and applied magnetic field. Inside a VSM, the samples were vibrated at a known frequency through a pick-up coil while being exposed to a steady, uniform background magnetic field (the applied field). The magnetic field may be generated by an electromagnet or a

superconducting magnet. The change in magnetic flux through the pick-up coil due to the vibration of the sample leads to a voltage across the pick-up coil, because of Faraday's law of induction. This voltage output is calibrated to yield the magnetization of the sample.

Computational Methods & Goals

The raw data for La-Fe-Si and CoMnSi consist of the magnetization at specific temperature and applied field intervals. To transform magnetization data into magnetic entropy data, the Maxwell Relation is applied:

$$\Delta S(T, \Delta H) = \int_0^{\Delta H} \left(\frac{\partial M}{\partial T}\right)_H dH \ . (8.1)$$

Here M is the magnetization, T is the temperature, ΔH is the change in applied magnetic field and ΔS is the change in entropy. The finite difference method was used to numerically determine $\left(\frac{\partial M}{\partial T}\right)_H$ at the given M points, shown in Eqs. (9.1-9.3).

$$Forward\ Difference: \Delta_h[M](T) = \frac{M(T+h) - M(T)}{T_{i+1} - T_i} \ (9.1)$$

$$Backward\ Difference: \nabla_h[M](T) = \frac{M(T) - M(T+h)}{T_i - T_{i-1}} \ (9.2)$$

$$Central\ Difference: \delta_h[M](T) = \frac{M(T+h) - M(T-h)}{2h} (9.3)$$

The central difference method was applied to the bulk of the data while forward and backward differences were applied at the endpoints of the data. The trapezoidal rule was then applied to these discretely calculated partial derivatives to calculate the final Maxwell Integral at various applied magnetic field strengths.

Two main parameters which characterize the potential of a material to be used in refrigerant applications are Refrigerant Capacity (RC) and hysteresis. RC and hysteresis were plotted as a function of applied magnetic field. This demonstrates how the material would behave in devices with a varying magnetic field, such as an Active Magnetic Regenerator (AMR). The efficiency of the magnetic material in terms of the energy transfer between the cold (T_{cold}) and hot (T_{hot}) reservoirs, is quantified by its RC:

$$RC\ (\Delta H) = \int_{T_{cold}}^{T_{hot}} \Delta S\ (T, \Delta H) dT. (10.1)$$

T_{cold} and T_{hot} are commonly selected as the temperatures corresponding to the full width at half maximum of ΔS_M. As stated previously, ΔS_M is magnetic entropy and is a function of magnetization. The RC can be calculated discretely at different points of the applied H-field. For example, separate refrigerant capacities can be calculated at the applied fields of 1, 2, 3, 4, and 5 Tesla.

A hysteresis loop quantifies the relationship between the magnetic flux (M) and magnetizing force

(H). To determine the entire area enclosed by the hysteresis loop, we use the following equation:

$$\int_{H_{Min}}^{H_{Max}} M\, dH = total\ area\ enclosed\ by\ hysteresis\ loop. \quad (11.1)$$

Due to the unavailability of decreasing field data for La-Fe-Si, we create hysteresis curves only for CoMnSi. In future work, data can be measured for La-Fe-Si to include decreasing field data.

Raw magnetization data were read into Python from comma separated value (CSV) files. Libraries such as matplotlib, numpy, pandas, scipy, and sympy were used for data analysis. To implement the analysis, I applied the Maxwell relation, and numerical differentiation and integration techniques. As outlined above, the program differentiates magnetization (M) with respect to temperature (T) at a constant magnetic field (H). To perform this differentiation, the
program used the finite difference technique, as shown in Eqs. (9.1-9.3). The program then integrates the result along H using the trapezoidal rule.

In addition to carrying out data analysis for this study, the code developed for this project could be distributed as magnetocaloric analysis software. I have created a workable portion of the software. When provided measurements of the magnetization of a material under different temperatures and applied magnetic fields, this portion can compute the entropy change of the material as it undergoes a change in applied field and create plots of the magnetization and entropy behavior of a material as a function of applied magnetic field and temperature.

Results

Table 1 shows several key magnetocaloric characteristics of La-Fe-Si and CoMnSi. The second column shows the applied H-field in units of Tesla. The third column shows the peak entropy change from 0 to the identified magnetic field as calculated by the Maxwell relation.

Material	$\mu_0\Delta H$ (T)	ΔS_{MAX} ($J^{-1}\ kg^{-1}$)	T_{Peak}(K)	δT_{FWHM} (K)	RC ($J\ kg^{-1}$)
La-Fe-Si	.4	-4.95	333	4.5	19.7
CoMnSi	1	.064	310	76	3.9
La-Fe-Si	.8	-11.99	334	4.8	47.30
CoMnSi	2.5	1.06	280	30	52.97
La-Fe-Si	1.6	-18.32	336	7.4	108.9
CoMnSi	5	4.79	235	29	215.4

Table 1. Derived magnetocaloric properties of La-Fe-Si and CoMnSi. **$\mu_0\Delta H$** refers to the change in the applied magnetic field, or H-field. **Δ_{SMAX}** refers to the peak change in entropy of the material while the magnetic field is applied. Peak width of temperature (T_{Peak}) was calculated at half height. Refrigerant capacity was calculated by integrating entropy curves at half height for each respective magnetic field.

La-Fe-Si displays a much larger ΔS_{MAX} and T_{Peak} than CoMnSi. In fact, La-Fe-Si demonstrates the G-MCE at room temperature. La-Fe-Si also has a greater T_{Peak} due to the presence of hydrogen, which was deliberately added to increase the T_{Peak} to above room temperature. CoMnSi exhibits a much larger δT_{FWHM}, or peak width since CoMnSi is a second order transition material at low fields while La-Fe-Si is not. Despite CoMnSi demonstrating the magnetocaloric effect over a broader temperature range, its ΔS_{MAX} is considerably smaller than La-Fe-Si. The magnetic field and temperature dependence of the magnetization behavior of La-Fe-Si and CoMnSi are summarized in Figure 1. The temperature dependence of the magnetization of La-Fe-Si is negative, meaning that La-Fe-Si loses magnetization as its temperature increases. CoMnSi, on the other hand, demonstrates little temperature dependence of magnetization. Conversely, the magnetization curves of La-Fe-Si demonstrate less *magnetic field* dependence. However, the magnetization curves of CoMnSi have a positive magnetic field dependence, meaning that CoMnSi gains magnetization as the applied field increases. Data were measured at different field and temperature intervals since the MCE occurs at different applied field ranges in varied materials. The 2D data series in Figure 1 are cross-sections of the 3D magnetization surface plots in Figure 2.

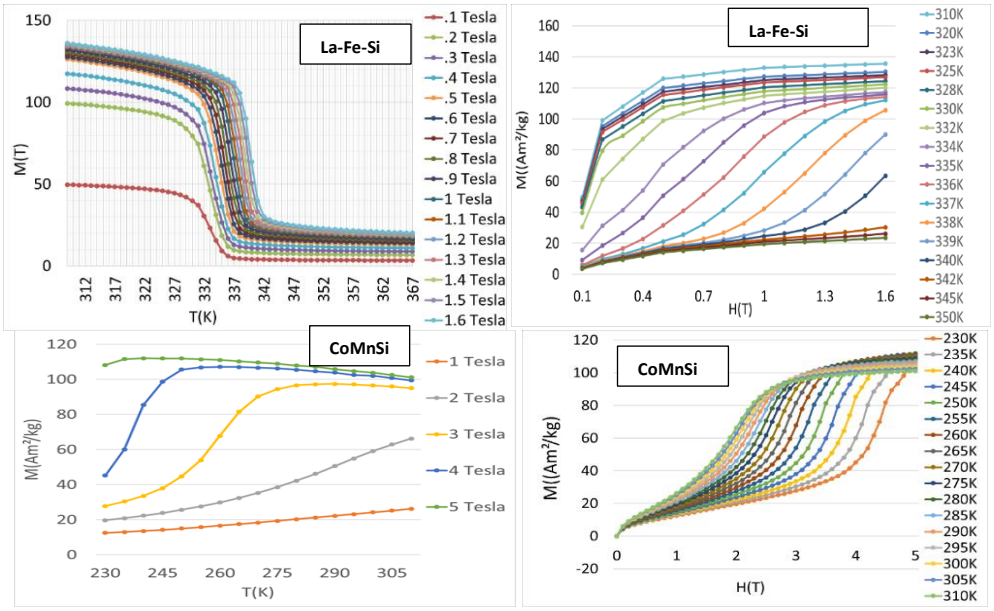

Figure 1. Magnetization cross-sectional curves of La-Fe-Si and CoMnSi. The first column of magnetization curves is a function of temperature in Kelvin, or T(K). The second column of magnetization curves is a function of H-field (applied magnetic field) in Tesla, or H(T). Am^2/kg is the SI unit of magnetization.

The peak width (along the temperature axis) for La-Fe-Si is 4.5 K at a field of .4 Tesla and then increases to 7.4 K in a field of 1.6 Tesla. The peak width appears to increase linearly as a function of applied field. This is important to note since peak width is used in refrigerant capacity calculations. Additionally, La-Fe-Si has a sharp change of lattice parameters whereas CoMnSi has a broad change of lattice parameters in these applied magnetic fields. This indicates that a larger applied field is necessary to achieve an optimal level of the magnetocaloric effect in CoMnSi than in La-Fe-Si. For example, La-Fe-Si reaches a magnetic saturation of

approximately 140 Am^2/kg at an applied field of 1.6 Tesla, while CoMnSi reaches a magnetic saturation of approximately 110 Am^2/kg at an applied field of 5 Tesla. Referring to the magnetic isotherm curves as a function of temperature, CoMnSi isotherms are flat while La-Fe-Si are peaked. The relative shapes of the magnetization curves can be observed in the 3D magnetization surface plots (Figure 2).

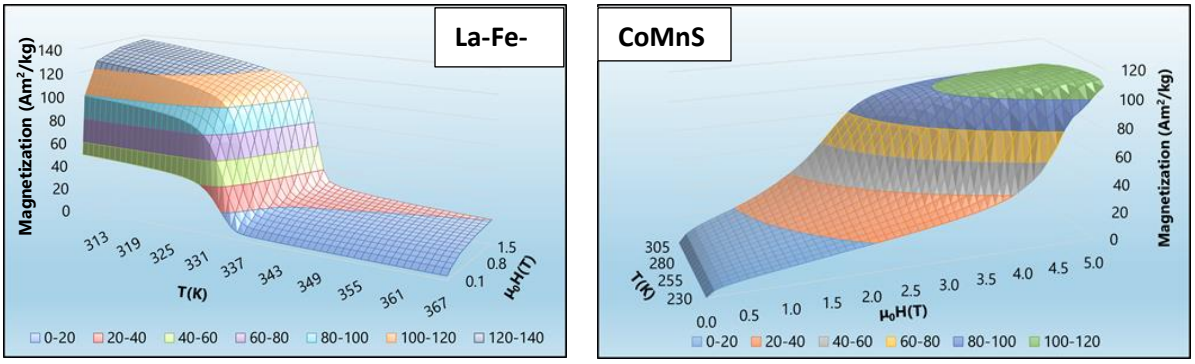

Figure 2. Three-dimensional visualizations of the isothermal magnetization behavior of La-Fe-Si and CoMnSi, respectively. The horizontal axes and vertical axes are different for each plot to properly illustrate the respective magnetic behaviors of each material. Refer to the line graphs in the Figure 1 for direct comparison of temperature and field dependent magnetization curves.

The Curie Temperature (T_C) can be graphically estimated for La-Fe-Si by several methods, which do not necessarily give results that agree within 1 K. For example, one way that the T_C can be determined is by observing the magnetization versus temperature and field plots in Figure 2. Graphically, we may say that the T_C is where a magnetic material reaches the inflection point of the downward M vs. T curve. The T_C in La-Fe-Si, or where temperature at which it becomes paramagnetic, is approximately 340K. Another means is to search for the peak in the ΔS curve at low fields. This occurs at approximately 335 K. Likewise, the transition temperature is ambiguous in CoMnSi, however, since there is an *upwards* M vs. T curve. In fact, it is not a Curie temperature but is instead a metamagnetic temperature at which a critical field induces a high magnetization state (Barcza et al., 2013).

The temperature of the inflection in magnetization in La-Fe-Si also shifts to the right as a greater magnetic field is applied (Table 1 and Figure 1). This means that as the applied magnetic field increases, the temperature at which the material magnetizes is greater. Consequently, the temperature at peak entropy shifts to the right for La-Fe-Si (Figures 3, 4, and 5). This shift is occurring due to a phase transition occurring at the given applied fields. If the maximum applied field was increased to larger fields such as 50 Tesla, then this shifting to the right would not be visible in graphs. The behavior for CoMnSi is the reverse, with the phase transition temperature decreasing as the applied field increases.

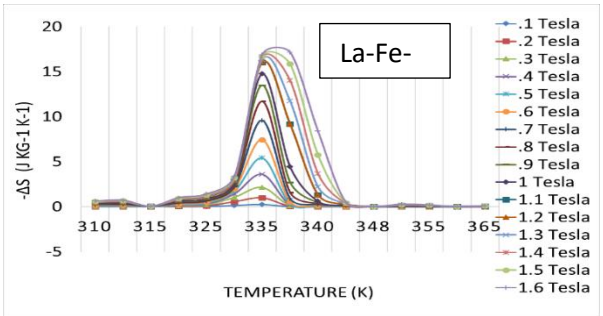

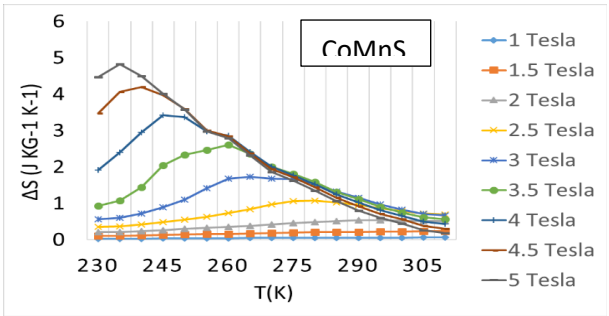

Figure 3. Entropy changes as a function of temperature for La-Fe-Si and CoMnSi while applied magnetic field is constant. Each entropy change curve corresponds to an applied magnetic field. La-Fe-Si undergoes a negative entropy change while CoMnSi undergoes a positive entropy change in an applied field (as indicated by the signs on the y-axis labels). The negative entropy change in La-Fe-Si is due to magnetic moment alignment in an external magnetic field. Negative entropy change in CoMnSi is stems from the presence of a change in the electronic density of states (Barcza et al., 2013). Differing magnetic properties of Co, Mn, and Si cause the material to undergo an overall *increase* in magnetic entropy because of the mixed magnetic behaviors.

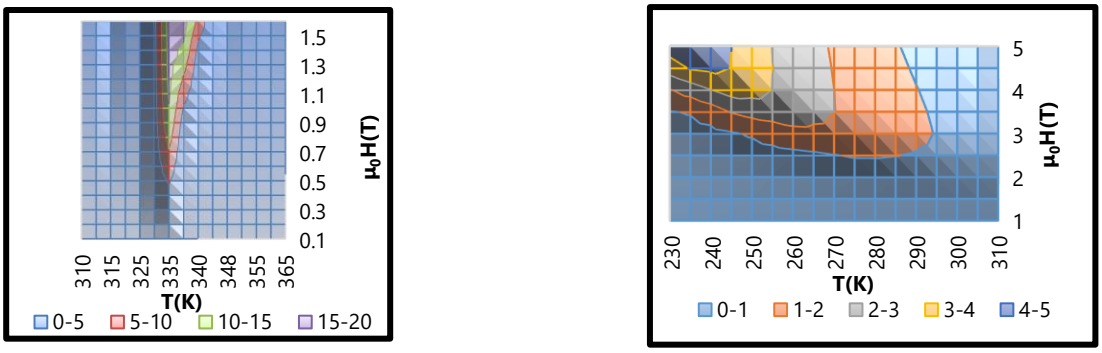

Figure 4. Two-dimensional data visualizations of the magnetic entropy behavior of La-Fe-Si and CoMnSi, respectively. The unit for magnetic entropy (the colored gradients) is J kg^{-1} K^{-1}. Note that the gradient for La-Fe-Si is ***positive*** while the gradient for CoMnSi is ***negative***. These gradients are a top-down perspective of the 3D surface plots presented in Figure 5.

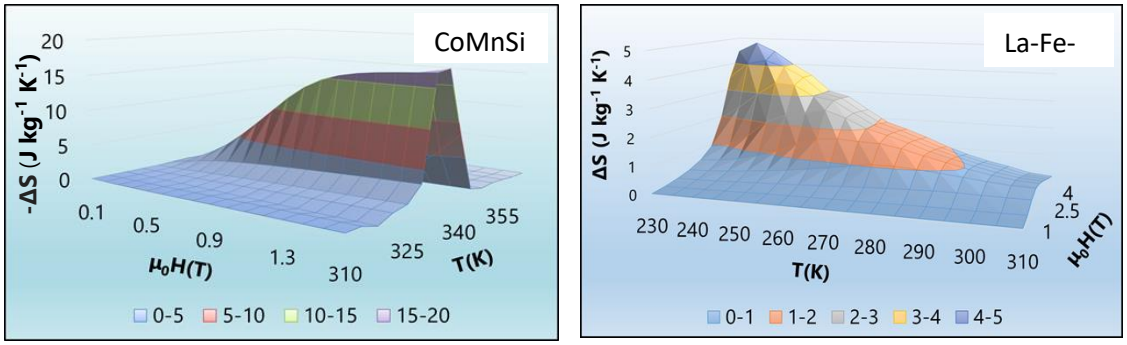

Figure 5. Three-dimensional data visualizations of the magnetic entropy behavior of La-Fe-Si and CoMnSi, respectively. Note the ***negative*** denotation on the y-axis of the La-Fe-Si plot. The x-axes and y-axes are different for each plot to best illustrate the respective entropy behaviors of the materials. To directly compare the entropy curve shapes, refer to the entropy line graphs.

The entropy change of La-Fe-Si is negative and steep, which means that the magnetic moments are aligned into a high magnetization state over a narrow applied magnetic field. However, the T_{Peak} changes only by a few Kelvin as the field increases. This contrasts with CoMnSi, where the T_{Peak} is affected greatly by the applied field, due to weaker entropy changes. CoMnSi therefore has a much larger peak width of 29K than 7.4 K for La-Fe-Si at the maximum applied fields of 5 T and 1.6 T, respectively. Since entropy change is a measure of the cooling effect (a high positive entropy suggests heating up in the magnetic field), also CoMnSi exhibits contrasting phase transition (Figure 6), hysteresis (Figure 7), refrigerant capacity (Figure 8) behaviors in comparison to La-Fe-Si.

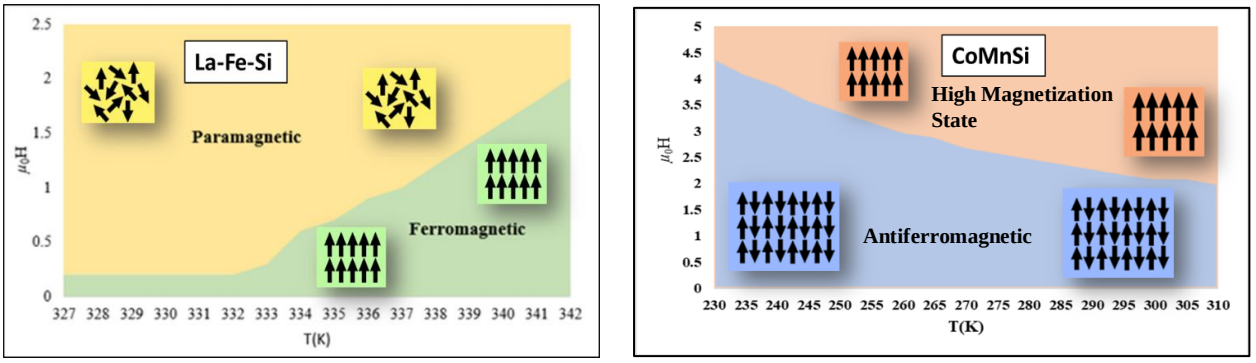

Figure 6. To generate phase diagrams, we apply a limit case of the Maxwell Relation, the Clausius-Clapeyron Equation for phase transitions: $\frac{dH}{dT} = \frac{\Delta S}{\mu_{0\Delta M}}$. (a) Representation of ferromagnetic-paramagnetic phase transition in La-Fe-Si, whereby the application of a high external magnetic field breaks ferromagnetic ordering. (b) Representation of the helical antiferromagnetic-high magnetization transition in CoMnSi which characterizes the suppression of the material's natural antiferromagnetic state.

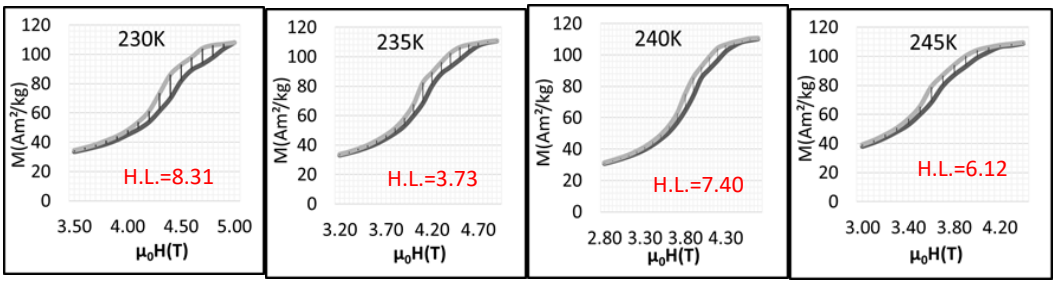

Figure 7. Magnetic hysteresis of CoMnSi when held at constant temperature. The darker line shows magnetization values when the field is applied while the lighter line shows magnetization behavior when the field is removed. μ_0H(T) represents the applied magnetic field in Tesla, while M refers to the magnetization of the material. Area under curve hysteresis losses (H.L), labeled in red, are expressed in the unit J/kg.

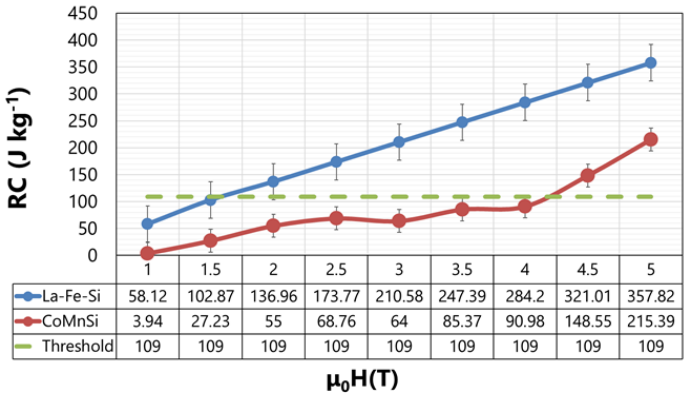

	1	1.5	2	2.5	3	3.5	4	4.5	5
La-Fe-Si	58.12	102.87	136.96	173.77	210.58	247.39	284.2	321.01	357.82
CoMnSi	3.94	27.23	55	68.76	64	85.37	90.98	148.55	215.39
Threshold	109	109	109	109	109	109	109	109	109

Figure 8. Plot of RC as a function of applied field. The data table on the bottom numerically compares these values. RC for La-Fe-Si was approximated through extrapolation from the 2T to 5T range. The 'Threshold' series indicates the maximum experimentally measured RC of La-Fe-Si. Refrigerant capacity is used to compare the potential effectiveness of materials in a magnetic refrigerator. The refrigerant capacity of CoMnSi given an applied field of 1.5 Tesla is approximately 27.3 J kg^{-1} while the refrigerant capacity of La-Fe-Si under the same applied field is approximately 102.9 J kg^{-1}. The refrigerant capacity for CoMnSi varies more strongly with magnetic field above a threshold field value. This is due to the second to first order transition at the tricritical point.

Hysteresis losses negatively affect effective refrigerant capacity. Hysteresis losses were not calculated for La-Fe-Si. However, the hysteresis losses for first order materials (such as La-Fe-Si) are almost always greater than the hysteresis losses for second order materials (Gutfleisch, et al., n.d.). In other words, CoMnSi shows little thermal irreversibility compared to other inverse magnetocaloric materials. This can be observed in hysteresis curves of figure 7. Unlike CoMnSi, detrimental hysteresis losses for La-Fe-Si occur due to the magnetization of the material. The irreversible energy loss directly lowers the efficiency of the magnetic refrigeration. Despite the moderate hysteresis effects, however, CoMnSi has a lesser utility for industrial applications, based on a lower refrigerant capacity.

AutoCAD Drawings of Magnetic Refrigeration Prototypes

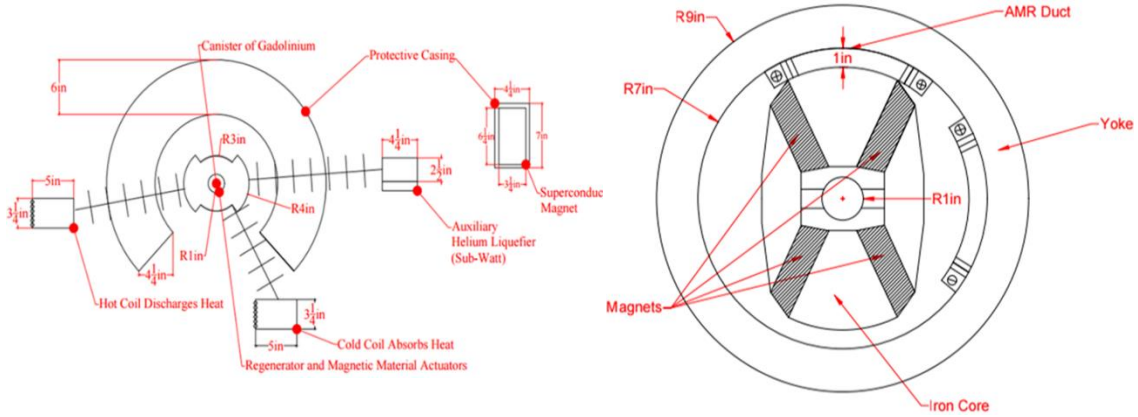

Figures 9 and 10. AutoCAD-generated cross-sections of proposed magnetic refrigerator prototypes with dimensions. The magnetocaloric material heats upon entry into the magnetic field and cools down upon exit. To obtain continuous efficiency, the magnetocaloric material enters and exits the external field periodically. Linear and rotational movements induce temperature changes in the material. (a) Linear reciprocating magnetic refrigerator consisting of a screen of conventional magnetocaloric material (e.g., Gadolinium or La-Fe-Si) placed within an electromagnetic field generated by a concave circular, superconducting magnet. Mechanical actuators enable hot and cold reservoirs to exchange thermal energy via helium liquefaction flow. This enables calculation of simple Carnot Efficiency: $\frac{T_H - T_C}{T_H}(100\%)$. (b) Rotary Active Magnetic Regenerator (AMR) consisting of a regenerator, magnet, and flow control system for heat exchange (the flow control system is the AMR duct). The material is placed inside the yoke encasing the unit and magnetized in the presence of permanent magnets circularly rotating magnets.

Construction of Magnetization Measurement/Magnetocaloric Effect Analysis Software

A package of software tools is built in the Python programming language to process experimental magnetization data. Experimental data consists of magnetization data values expressed as a function of temperature of the material system and the external applied magnetic field, as displayed in Figure 8. Three main parameters of the experimental system are characterized by the software, in order of computation, are graphical visualization of raw magnetization data, graphical visualization and determination of magnetic entropy of the sample, and differential susceptibility of the sample. Raw magnetization data is provided in the form of .CSV or an analogous text file. The user interface of the program is created via cell blocks in the Jupyter notebook where each cell block contains a specific calculation or visualization command that the user could call to generate analysis.

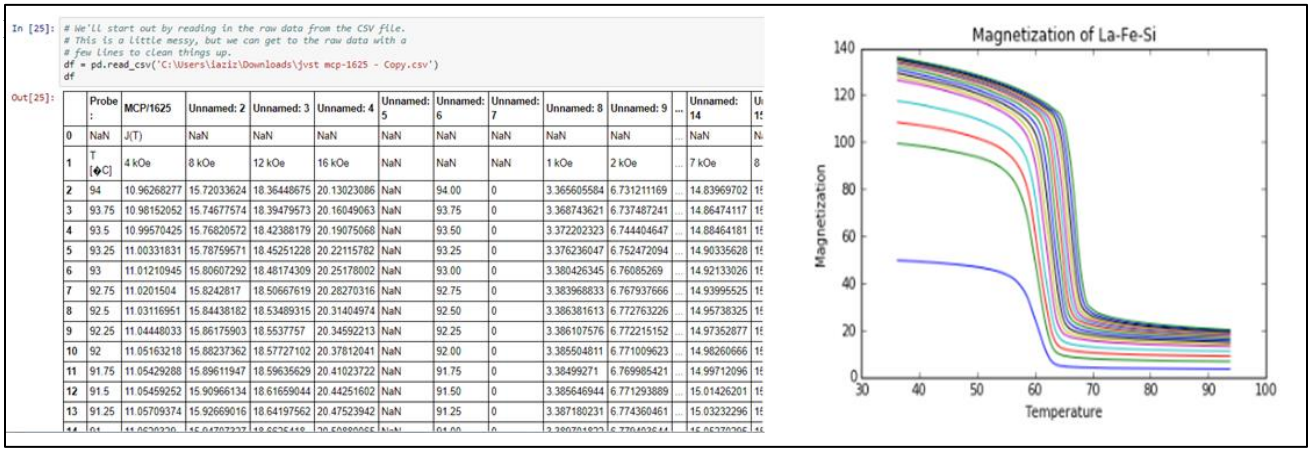

	Probe :	MCP/1625	Unnamed: 2	Unnamed: 3	Unnamed: 4	Unnamed: 5	Unnamed: 6	Unnamed: 7	Unnamed: 8	Unnamed: 9	...	Unnamed: 14	U 15
0	NaN	J(T)	NaN	NaN	NaN	NaN	NaN	NaN	NaN	NaN	...	NaN	Na
1	T [◆C]	4 kOe	8 kOe	12 kOe	16 kOe	NaN	NaN	NaN	1 kOe	2 kOe	...	7 kOe	8
2	94	10.96268277	15.72033624	18.36448675	20.13023086	NaN	94.00	0	3.365605584	6.731211169	...	14.83969702	15
3	93.75	10.98152052	15.74677574	18.39479573	20.16049063	NaN	93.75	0	3.368743621	6.737487241	...	14.86474117	15
4	93.5	10.99570425	15.76820572	18.42388179	20.19075068	NaN	93.50	0	3.372202323	6.744404647	...	14.88464181	15
5	93.25	11.00331831	15.78759571	18.45251228	20.22115782	NaN	93.25	0	3.376236047	6.752472094	...	14.90335628	15
6	93	11.01210945	15.80607292	18.48174309	20.25178002	NaN	93.00	0	3.380426345	6.76085269	...	14.92133026	15
7	92.75	11.0201504	15.8242817	18.50667619	20.28270316	NaN	92.75	0	3.383968833	6.767937666	...	14.93995525	15
8	92.5	11.03116951	15.84438182	18.53489315	20.31404974	NaN	92.50	0	3.386381613	6.772763226	...	14.95738325	15
9	92.25	11.04448033	15.86175903	18.5537757	20.34592213	NaN	92.25	0	3.386107576	6.772215152	...	14.97352877	15
10	92	11.05163218	15.88237362	18.57727102	20.37812041	NaN	92.00	0	3.385504811	6.771009623	...	14.98260666	15
11	91.75	11.05429288	15.89611947	18.59635629	20.41023722	NaN	91.75	0	3.38499271	6.769985421	...	14.99712096	15
12	91.5	11.05459252	15.90966134	18.61659044	20.44251602	NaN	91.50	0	3.385646944	6.771293889	...	15.01426201	15
13	91.25	11.05709374	15.92669016	18.64197562	20.47523942	NaN	91.25	0	3.387180231	6.774360461	...	15.03232296	15

Figure 8. Inputted raw magnetization data (left) indexed by temperature (column "probe") and field (row 1) labels is converted into magnetic flux curve visualizations (right).

Here, we successfully test the initial component of the software based on experimental magnetization measurements of La-Fe-Si. The initial component of program formats the data frame by recognizing and indexing metadata (e.g., temperature and applied field labels). Specifically, the given tables of strings are converted to float arrays. After this metadata is processed, the numpy and scipy libraries' built-in functions for differentiation and integration are enabled.

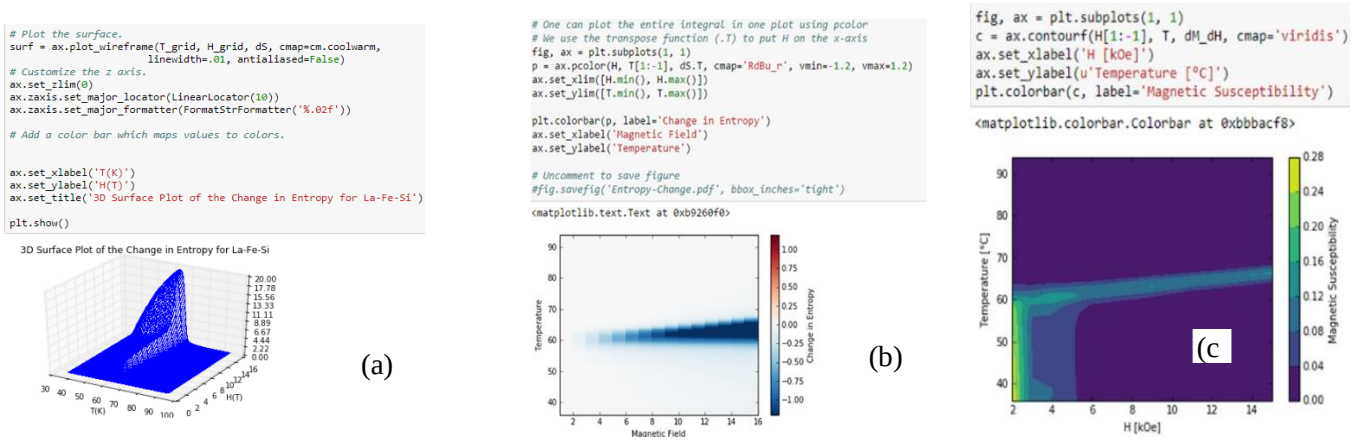

Figure 9. Entropic work output is visualized in the form of caloric entropy variations (ΔS). (a) Wireframe surface representation of magnetic entropy changes in La-Fe-Si. (b) Gradient cross-section representation of magnetic entropy changes in La-Fe-Si. (c) Gradient cross-section representations of differential magnetic susceptibility in La-Fe-Si.

The Maxwell Relations express the change in magnetization of the material as a function of work output affected by the external magnetic field and temperature. The program numerically estimates this work output using the numerical differentiation and integration techniques defined below. Entropy (ΔS) is defined as $\Delta S = \int_{H_1}^{H_2} \left(\frac{\partial M}{\partial T}\right)_H$, where numerical approximation techniques are employed at defined temperature and applied field intervals. The software assumes that all other thermodynamic variables, such as pressure, are constant. The finite difference method is used within the program to numerically determine $\left(\frac{\partial M}{\partial T}\right)_H$ at the given M points, as shown in Eqs (9.1-9.3).

Differential magnetic susceptibility χ_{ij}^{d} is calculated as the tensor $\chi_{ij}^{d} = \left(\frac{\partial M_i}{\partial H_j}\right)_H$ where M_i and H_j are perpendicular components of magnetization and applied magnetic field. The tool illustrates regions of relative intensity in the form of gradients, where localized electron moments are strongly affected by an, or susceptible to, external magnetic field. Along with caloric entropy changes, magnetic susceptibility curves are integrated to quantify potential implementation into industrial applications such as spin transistors. Elevated levels of magnetic susceptibility indicate that the parameters domain wall configuration and the correlated electron system's spin directions are strongly affected by an external field. Regions of high intensity indicate the relative contribution of an external magnetic field term to the internal exchange interactions which occur between neighboring spin moments.

Investigation on the Derivation of the Heisenberg Spin Hamiltonian

The Heisenberg Spin Hamiltonian is an operator corresponding to the total kinetic energy of a single-body system, where H is the sum of the kinetic energies of interacting particles and the potential energy of those in the system. Thus, this Hamiltonian is derivable as a function of spin couplings. If a lattice contains N electron sites, where each lattice site contains a defined spin value, then the total Hilbert Space in which the physical state lies is $H = \bigotimes^{N} C^2$. C is the vector space of all real or complex convergent sequences.

Given two neighboring i and j sites, we denote the exchange interaction as the outer product of spin operators S_i and S_j and the scalar exchange constant (J):

$$H_{ex} = \sum_i S_i J_{ij} S_j = \sum_i S_i J_{ij} S_{i+1} = \sum_i J_x S_i^x S_{i+1}^x + J_y S_i^y S_{i+1}^y + J_z S_i^z S_{i+1}^z. \quad (12.1)$$

We now define a local coordinate system from these operators given that $\theta_n = QP_n$ is the angle of an arbitrary spin moment given the magnetic ordering vector Q and lattice position P_n so $S_{nj} = R_n S_{0j}$ where R_n is a rotation matrix dependent upon θ_n.

To solve the exchange Hamiltonian, we define the following coordinate transformation:

$$S_i^{\alpha} = \sum_{\mu} R_i^{\alpha} J_i S_i^{\mu} = R_i S'_{nj} + R'_j S''_{nj}. \quad (13.1)$$

This transformation expresses spin operator S_i^{μ}, which defines subsequent spin values in the local coordinate system. α and μ runs over $\{x, y, z\}$. Given this spin vector, the rotation matrix R relates the spin on the S'_{nj} and S''_{nj} subsequent sites.

Since this work is interested in extended arrays of spin, the symmetries of the Hamiltonian with respect to rotations in spin space, we must consider cases where the Hamiltonian is <u>not</u> invariant under continuous rotations. Terms which violate invariance under rotations in spin space are anistropic (H_{an-ex}). Anistropic exchange manifests as inconsistent symmetric couplings in spin space, mathematically defined as:

$$H_{an-ex} = \sum_{i<j} J_{ij}^{xy}\left(S_{ix}S_{jx} + S_{iy}S_{jy}\right) + S_{ij}^{z}S_{iz}S_{jz.} \text{ (14.1)}$$

The final term in the Hamiltonian considers the effect of an external field vector H on spin coupling. The external field couples as $H_{H_{field}} = H_{field}\sum_i S_i$. Given that the magnetic flux, M, is $\sum_i \mu_i S_i$, we expand H_{field} to include the Bohr Magneton, μ_B, the magnetic moment of an electron, and the g-tensor*, g.* The tensor accounts for the anisotropy, inherent in that vector H_{field} defines a special dimension in space:

$$H_{H_{field}} = \sum_i \mu_B H_{field} gS = \mu_B[H_x \quad H_y \quad H_z]\begin{bmatrix} g_{xx} & g_{xy} & g_{xz} \\ g_{yx} & g_{yy} & g_{yz} \\ g_{zx} & g_{zy} & g_{zz} \end{bmatrix}\begin{bmatrix} S_x \\ S_y \\ S_z \end{bmatrix}. \text{(15.1)}$$

The resultant term, the *total Hamiltonian*, is the sum of the H_{ex}, H_{an-ex}, and $H_{H_{field}}$ terms. The anisotropy term in Eq. (15.1) is rewritten with an A_{ni} matrix to define asymmetric couplings in spin space:

$$\boldsymbol{H = \sum_{mn,nj} S_{mi}J_{mi,nj}S_{nj} + \sum_{mi} S^{T}{}_{mi}A_{ni}S_{mi} + \mu_B H^{T}\sum_{mi} g_i S_{mi}.\ (16.1)}$$

Since the Hamiltonian for such a system is naturally built out of spin operators, we define two vectors:

$$w_i^{\alpha} = R_i^{\alpha\,1} + iR_i^{\alpha\,2} \text{ (17.1) and } z_i^{\alpha} = R_i^{\alpha\,3}. \text{(17.2)}$$

z_i^{α} is a unit vector parallel to the net magnetic moment of the i^{th}-atom within the unit cell. The Spin Hamiltonian for such a many-body system is built out of the spin operators (S_{ix}, S_{iy}, S_{iz}) and we can transform the given w_i^{α} on the quantum basis states in Eqs. (18.1-18.4) using bra-ket notation

$$\langle \hat{s}_i^3 | S_i^3\rangle = S_i^3|\grave{S}_i^{3\grave{}}\rangle_i \text{ (18.1)} \qquad \hat{s}_{mi}^{+}|\hat{s}_{mi}^{3}\rangle_i = \sqrt{S(S+1) - S_i^3(S_i^3+1)}\; S_i^3 + 1\rangle_i \text{ (18.2)}$$

$$\hat{s}_{mi}^{+}|\hat{s}_{mi}^{3}\rangle_i = \sqrt{S(S+1) - S_i^3(S_i^3+1)}|S_i^3+1\rangle_i \text{ (18.3)} \qquad \hat{s}_{mi}^{+}|\hat{s}_{mi}^{3}\rangle_i = \sqrt{S(S+1) - S_i^3(S_i^3-1)}|S_i^3-1\rangle_i \text{ (18.4)}$$

Note that for any particle with spin quantum number S, the number always assumes one of $2S+1$ possible values within the set: $\{-S, -S+1, \ldots, S-1, +S\}$, so that there exists $(2N+1)$ basis states given N sites.

Spins in finite-dimensional Hilbert space exhibit boson-like behavior. Thus, operators from different spin matrices commute. This symmetry to spin operators is naturally exploited by the Holstein-Primakoff bosonization technique, where spin operators are replaceable by boson annihilation operators in Eqs. (19.1-19.3) expressed with the reduced Planck constant $\hbar$.

$$s_{mi}^{+} = \hbar\sqrt{2S}\sqrt{1 - \tfrac{b_{mi}^{+}b_{mi}}{2S}}b_{mi} \text{ (19.1)} \qquad s_{mi}^{-} = \hbar\sqrt{2S}b_{mi}^{+}\sqrt{1 - \tfrac{b_{mi}^{+}b_{mi}}{2S}} \text{ (19.2)} \qquad s_{mi}^{3} = \hbar(s - b_{mi}^{+}b_{mi}) \text{ (19.3)}$$

This simplifies in the spin operators in Eqs. 20.1-20.3 implemented by the MATAB toolbox SpinW (Toth & Lake, 2015), which evaluates the Hamiltonian, where b_{mi} and b_{mi}^{+} are boson annihilation and creation operators, respectively.

$$s_{mi}^{+} = \sqrt{2S}b_{mi} \;\; s_{mi}^{-} = \sqrt{2S}b_{mi}^{+} \text{ (20.1)}$$

$$s_{mi}^{1} = \frac{\sqrt{2S_i}}{2}(b_{mi} + b_{mi}^{+})\ (20.2)\ s_{mi}^{2} = \frac{\sqrt{2S_i}}{2}(b_{mi} - b_{mi}^{+})\ (20.3)\ s_{mi}^{3} = (S_i - b_{mi}^{+} b_{mi})\ (20.4)$$

As it applies to the interaction parameters, the Monte Carlo Method relies on repeated random sampling to account for the many coupled degrees of freedom in the spin Hamiltonian. In the spin Hamiltonian, the number of degrees of freedom refers to the number of exchange parameters that vary independently.

Quantum Mechanical Description of Magnetocaloric Effects in Gadolinium

We generate an atomistic model of magnetocaloric effects in the 2nd order ferromagnetic nanomaterial Gadolinium by defining pairwise exchange energy (J_{ij}) between atoms of neighbor-index in the C++ VAMPIRE library (Evans et al., 2014). The MATLAB quantum magnetism toolbox SpinW is used to impose magnetic interactions on the crystal structure, given J_{ij} and μ_S(spin moment) of 3.5. The crystal structure of Gadolinium is hexagonal close packed (HCP) with a P63 space group. Applying the built-in mathematical representations of the HCP and P-63 geometric space groups in SpinW, we plot the structure in Figure 10.

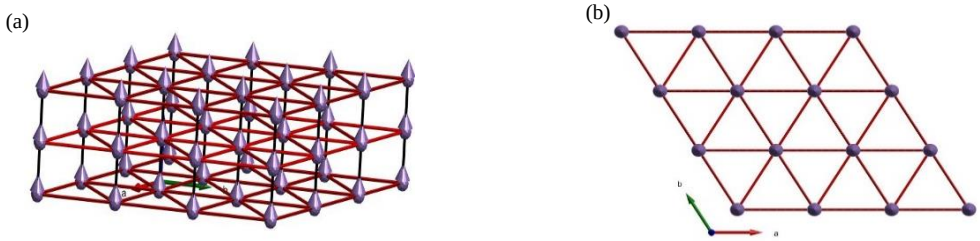

Figure 10. Atomic spatial visualizations of the ordered crystal structure within Gadolinium at its optimized ground state as calculated in SpinW. (a) 3-dimensional ferromagnetic lattice where spin alignments are parallel in the a-b plane. (b) Singular lattice layer plane consisting of Gd^{+} atoms.

Nearest-neighbor ferromagnetic exchanges (J_{ij}) are determined by the meanfield expression, $J_{ij} = \frac{3K_B T_C}{\varepsilon z}$, where K_B is the Boltzmann constant. Given $J_{ij} = 5.9\ meV$, we match the experimentally known T_C of 294K by adjusting the spin fluctuation factor (ε) to .95 from the expected value of .790 for the HCP structure. The HCP structure, as plotted in Figure 14, contain four atoms per unit cell resulting in a coordination number (z) of 12. VAMPIRE maps operators in Eqs. (18.1-18.4) to the Hamiltonian in Eq. (16.1) by using the Monte-Carlo Method to generate magnetization data (Evans et al., 2014). The external field tensor ($\mu_B H^T \sum_{mi} g_i S_{mi}$) in Figure 11 is defined up to $H^T = 5\ T$.

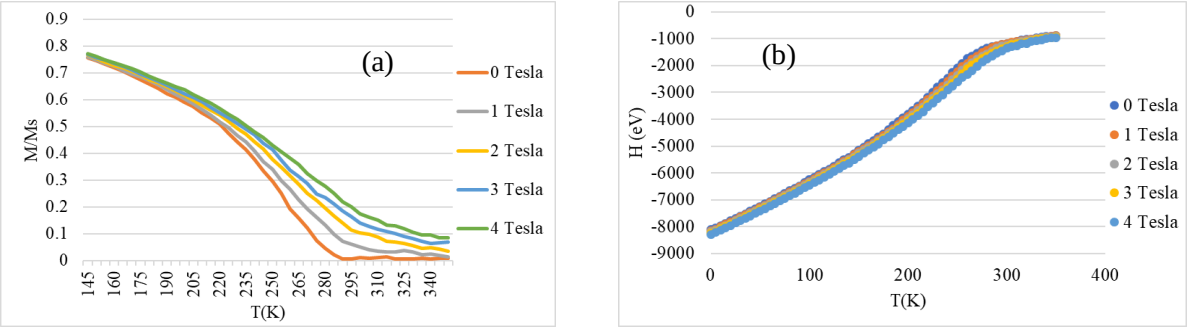

Figure 11. (a) Magnetization $\left(|\boldsymbol{m}| = \frac{\sum_i \mu_i S_i}{\sum \mu_i}\right)$ cross-sectional curves of Gadolinium as a function of temperature in Kelvin. M/M_S denotes the normalized sum of spin moments with respect to saturation magnetization (M_S). Increased magnitudes of the external magnetic field induce a higher magnetic ordering critical point (T_C). (b) Total energy term ($\boldsymbol{H} = \sum_{mn,nj} \boldsymbol{S}_{mi} \boldsymbol{J}_{mi,nj} \boldsymbol{S}_{nj} + \sum_{mi} \boldsymbol{S}^T{}_{mi} \boldsymbol{A}_{ni} \boldsymbol{S}_{mi} + \boldsymbol{\mu_B} \boldsymbol{H}^T \sum_{mi} \boldsymbol{g}_i \boldsymbol{S}_{mi}$) of the Hamiltonian corresponding to the external magnetic field deviations from the ground state $H=0$. At the T_C, we note an inflection point in the total energy curve, indicating that exchange interactions ($H_{ex} = \sum S_i J_{ij} S_j$) reach a constant non-zero magnitude in the paramagnetic phase.

Experimental Thermocouple Set-Up in Gadolinium

The following is an experimental demonstration set-up of the magnetocaloric effect in Gadolinium. A 100-gram sample of Gadolinium was used. Gadolinium is a rare-earth metal which demonstrates the conventional magnetocaloric effect whereby its temperature increases when it enters the magnetic field and decreases when it leaves the magnetic field. The magnetocaloric effect in Gadolinium occurs near room temperature (68 °F), which makes the material ideal for demonstration purposes. Prior to exposing Gadolinium to a magnetic field, its temperature was measured using the Dual-channel Leaton Digital Thermocouple Thermometer, labeled in Figure 12. Two dissimilar metals are joined as a circuit, and thus, a thermocurrent is generated from the temperature difference between the metals. If there is a temperature difference between the thermocouple tip and the reference end of the thermocouple, the instrument will display the temperature value of the material being tested. In this demonstration, two different thermocouples are connected to a single thermometer. This enables the thermometer to display two different temperature outputs which indicate the temperature of Gadolinium at two points on its surface.

Figure 12. Image on the left is the experimental demonstration set-up of the magnetocaloric effect in Gadolinium. Images on the right are close-up photographs of the Gadolinium used in this demonstration and modelled in the VAMPIRE C++ Library. After the surface temperature of Gadolinium is measured (when it is not exposed to a magnetic field), the material is placed in an applied magnetic field. In this case, Gadolinium was exposed to a static magnetic field using permanent magnets, as shown. Here, the magnetic field was generated from the spin of electrons within the material itself. These permanent magnets generated an applied magnetic field of approximately 2.2 Microtesla. Alternatively, an electromagnet could be used where the magnetic field is generated as an electric current is applied. After Gadolinium was exposed to a magnetic field of 2.2 Microtesla, it was removed from it. As expected, Gadolinium experienced a temperature decrease as it was removed from an applied field. To measure the strength of the magnetic field, a vector magnetometer is utilized.

Discussion and Conclusions

Results presented here enable researchers to compare properties of the conventional and inverse magnetocaloric effects. By taking the first-order conventional magnetocaloric material La-Fe-Si and comparing it to the second-order inverse magnetocaloric material CoMnSi, we apply observations to general explanations of behavior by constructing a micromagnetic spin model. We draw conclusions on the industrial applications for each. Software we created are designed to be used in future research.

Overall, the expected outcome was supported by the data in that La-Fe-Si is a more suitable candidate than CoMnSi for industrial applications. This because La-Fe-Si demonstrates the G-MCE over a very narrow temperature interval, meaning that La-Fe-Si would go into a heating state very quickly. CoMnSi, on the other hand, magnetizes very slowly as a function of applied field. La-Fe-Si also has a greater T_{Peak} because of the presence of hydrogen. This greater T_{Peak} makes La-Fe-Si better suited to room-temperature applications.

CoMnSi has smaller entropy changes and refrigerant capacities than most conventional MCMs (e.g., La-Fe-Si) at comparable magnetic fields, yet demonstrates advantageous characteristics for use in refrigeration applications. By undergoing a change in the electronic density of states, CoMnSi has a broadened transition in temperature and a reduced effective hysteresis. This broadened transition in temperature allows CoMnSi to be used in cooling devices where cooling is needed over a wide range of temperatures. Although multiple conventional MCMs with consecutive smaller temperature transitions could be used together (accounting to a broad overall temperature transition), using multiple materials may not be cost effective.

The micromagnetic model built at an interface between MATLAB (via SpinW) and C++ (via VAMPIRE) generates quantification of spin-induced magnetic interaction parameters (e.g., spin waves corresponding to the total energy Hamiltonian) underlying emergent thermodynamic observables such as adiabatic demagnetization. Since these spin waves carry pure spin currents in the absence of electron flow, the possibility of using waves instead of particles for computing enables new device concepts for spin processing such as spin logic gates and transistors. As a first step towards achieving practical realization of magnon-based computing, it is necessary to encode binary data into spin waves. To realize a computing device based on spin, our model may be used to simulate the control of spin polarization modes via external fields by plotting the total energy Hamiltonian. Control of spin polarization will enable logical operations on

encoded data.

To carry out the comparison of MCEs, I developed software, which can perform mathematical analysis, in Python. This software can be used as a simulation of the magnetocaloric effect given an anticipated magnetization data set. Here, the software would predict material behavior in industrial or commercial magnetic refrigerators. The software can also be used to directly analyze data from experimental tests of a magnetic refrigerator. Although I have already created a workable portion of the software, I am currently creating new code which include hysteresis and refrigerant capacity analysis and generate interactive three-dimensional surface plots. Another addition to the program which is being considered is the incorporation of real-time data from experiments. Here, the software would generate time series and plots in real time as the magnetization data is collected from the experiment.

Further studies will likely examine other possible inverse magnetocaloric materials, as these materials are rare relative to conventional MCMs. Construction of Hamiltonian-based spin models will provide predictions of emergent magnetic behaviors present in AMR devices based on magnetization measurements collected from VSMs and spin parameters. From an applied perspective, future work could investigate devices which use conventional and inverse magnetic materials in experimental refrigeration prototypes. Such studies could provide insight on how to combine the advantageous material characteristics of CoMnSi with the G-MCE of La-Fe-Si.

References

Addison, S. R. (n.d.). Thermodynamic Potentials and Maxwell's Relations. Retrieved from *http://faculty.uca.edu/saddison/Thermal2003/ThermodynamicPotentials.pdf*

Appelbaum, I., Huang, B., & Monsma, D. J. (2007, May 17). Electronic measurement and control of spin transport in silicon. Retrieved May 27, 2017, from *https://www.ncbi.nlm.nih.gov/pubmed/17507978*

Barcza, A., Gercsi, Z., Michor, H., Suzuki, K., Kockelmann, W., Knight, K. S., & Sandeman, K. G. (2013, February 08). Magnetoelastic coupling and competing entropy changes in substituted CoMnSi metamagnets. *Physical Review B, 87*(6). doi:10.1103/physrevb.87.06441

Blundell, S. J. (2014). Magnetism in condensed matter. Oxford: Oxford University Press.

Cheng, R., Daniels, M. W., Zhu, J., & Xiao, D. (2016). Antiferromagnetic Spin Wave Field- Effect Transistor. Nature, 6(1). *doi:10.1038/srep24223*

Cornell Physics. (n.d.). Spin Waves. Retrieved from *http://www.lassp.cornell.edu/clh/p654/5.5.pdf*

Cornell University. (n.d.). Spin Hamiltonians and Exchange interactions. Retrieved from *http://www.lassp.cornell.edu/clh/p654/MM-Lec0.pdf*

Du, A., & Du, H. (2005, May 17). Monte Carlo calculation of the magnetization behavior and the magnetocaloric effect of interacting particles. Journal of Magnetism and Magnetic Materials, 299(2), 247-254. doi:10.1016/j.jmmm.2005.04.011

Evans, R. F., Fan, W. J., Chureemart, P., Ostler, T. A., Ellis, M. O., & Chantrell, R. W. (2014). Atomistic spin model simulations of magnetic nanomaterials. Journal of Physics: Condensed Matter, 26(10), 103202. doi:10.1088/0953-8984/26/10/103202

Franco, V., Blázquez, J. S., Ingale, B., & Conde, A. (2012). The Magnetocaloric Effect and Magnetic Refrigeration Near Room Temperature: Materials and Models. Annual Review of Materials Research, 42(1), 305-342.

Franco, V. (n.d.). Determination of the Magnetic Entropy Change from Magnetic Measurements. Retrieved from *http://www.lakeshore.com/Documents/MagneticEntropyChangefromMagneticMeasurements.pdf*

Guillou, F., Porcari, G., Yibole, H., Dijk, N. V., & Brück, E. (2014, February 22). Taming the First-Order Transition in Giant Magnetocaloric Materials. *Adv. Mater. Advanced Materials, 26*(17), 2671-2675. doi:10.1002/adma.201304788

Gutenberg, P. (n.d.). Schwarz theorem. Retrieved from *http://www.gutenberg.us/articles/schwarz_theorem*

Gutfleisch, O., Gottschall, T., Fries, M., Benke, D., Radulov, I., Skokov, K. P., . . . Farle, M. (n.d.). Mastering hysteresis in magnetocaloric materials.

Khan, M., Ali, N., & Stadler, S. (2007, March 15). Inverse magnetocaloric effect in ferromagnetic Ni50Mn37xSb13−x Heusler alloys. Journal of Applied Physics, 101(5), 053919. doi:10.1063/1.2710779

Kitanovski, A., Plaznik, U., Tomc, U., & Poredoš, A. (2015). Present and future caloric refrigeration and heat-pump technologies. International Journal of Refrigeration. doi:10.1016/j.ijrefrig.2015.06.008

Kochmański, M., Paszkiewicz, T., & Wolski, S. (2013, July 22). Curie–Weiss magnet—a simple model of phase transition. European Journal of Physics. doi:10.1088/0143-0807/34/6/1555

Krenke, T., Duman, E., Acet, M., Wassermann, E. F., Moya, X., Mañosa, L., & Planes, A. (2005). Inverse magnetocaloric effect in ferromagnetic Ni–Mn–Sn alloys. *Nature materials*, *4*(6), 450-454.

Maxwell Relation. (2013, May 09). Retrieved from *https://thermodynamics-engineer.com/maxwell-relation/*

M.I.T. (2013). Maxwell Relations: A Wealth of Partial Derivatives. Retrieved from *https://ocw.mit.edu/courses/physics/8-044-statistical-physics-i-spring-2013/readings-notes-slides/MIT8_044S13_notes.Max.pdf*

Pecharsky, V. K., & Gschneidner Jr., K. A. (1999). Magnetocaloric effect and magnetic refrigeration. *Journal of Magnetism and Magnetic Materials, 200*(1-3), 44-56. doi:10.1016/s0304-8853(99)00397-2

Sheremet, A. S., Kibis, O. V., Kavokin, A. V., & Shelykh, I. A. (2016). Datta-and-Das spin transistor controlled by a high-frequency electromagnetic field. Physical Review B, 93(16), 165307.

Schekochihin, A. (n.d.). Classification of phase transitions. Retrieved from *https://www-thphys.physics.ox.ac.uk/people/AlexanderSchekochihin/A1/2011/handout13.pdf*

Smith, A. (2013). Who discovered the magnetocaloric effect? *The European Physical Journal H EPJ H, 38*(4), 507-517. doi:10.1140/epjh/e2013-40001-9

Toth, S., & Lake, B. (2015). Linear spin wave theory for single-Q incommensurate magnetic structures. Journal of Physics: Condensed Matter, 27(16), 166002.